

A Light-Powered Ultralight Tensegrity Robot with High Deformability and Load Capacity

Zhijian Wang, Kai Li, Qiguang He, and Shengqiang Cai*

Traditional hard robots often require complex motion-control systems to accomplish various tasks, while applications of soft-bodied robots are limited by their low load-carrying capability. Herein, a hybrid tensegrity robot composed of both hard and soft materials is constructed, mimicking the musculoskeletal system of animals. Employing liquid crystal elastomer–carbon nanotube composites as artificial muscles in the tensegrity robot, it is demonstrated that the robot is extremely deformable, and its multidirectional locomotion can be entirely powered by light. The tensegrity robot is ultralight, highly scalable, has high load capacity, and can be precisely controlled to move along different paths on multiterrains. In addition, the robot also shows excellent resilience, deployability, and impact-mitigation capability, making it an ideal platform for robotics for a wide range of applications.

Conventional robots are usually entirely composed of hard materials and require complex motion-control systems to accomplish different tasks. In particular, with the rigid components, most hard robots are not friendly in close contact with people or fragile objects.^[1] Recently, soft-bodied robots with high dexterity and deformability have been extensively explored, such as pneumatic soft robots,^[2–4] wearable soft robotic rehabilitation devices,^[5] and reaction-powered octopus-shaped soft robot,^[6] biomimetic photoinduced grippers,^[7,8] etc. However, poor load-carrying ability of soft-bodied robots often limits their real applications.^[9] For instance, very careful design is needed to construct an untethered soft robot which can move on the ground while carries its own weight and power supply.^[10] In nature, most terrestrial animals develop musculoskeletal systems, which are composed of both stiff bones and active and stretchable muscles, to achieve excellent dexterity and adaptivity while maintaining high load capacity.^[11,12] Inspired by

the musculoskeletal system, in this article, we design a novel hybrid tensegrity robot which is composed of both stiff struts and soft artificial muscle fibers.

By definition, a tensegrity structure is composed of compressive stiff struts and tensional soft cables, which is highly deployable, resilient and able to dissipate large impacting energy.^[13] Tensegrity robots have been recently proposed and built as the next generation robots for space exploration, which are typically actuated either by electrical actuators,^[14–16] pneumatic McKibben actuators,^[17,18] or shape memory alloys.^[19] Those actuation mechanisms are usually bulky, heavy and noisy, which may also require complex

controlling systems. It is still very challenging to construct an ultralight tensegrity robot with high deformability and loading capacity but simple actuation systems.


In the current work, we employ stiff plexiglass rods as the compressive struts and artificial muscle fibers as the tensional cables to construct a prototype of light-powered tensegrity robot, which closely resembles musculoskeletal structure of animals. The artificial muscle fiber is made up of liquid crystal elastomer (LCE)–carbon nanotube (CNT) composite (Figure S1, Supporting Information), which can generate large and reversible light-actuated deformation,^[20,21] and thus enables light-powered motion of the tensegrity robot. We will demonstrate that the tensegrity robot developed in the current work is ultralight, greatly deformable, highly scalable, has high load capacity and its rolling pathway can be entirely and precisely controlled by light irradiation.

The six-strut tensegrity robot is shown in **Figure 1A**. Six plexiglass rods of different colors are used as stiff struts, while 24 LCE–CNT composite fibers are used as tensional cables, which can exhibit large contraction in response to near-infrared (NIR) laser irradiation. All the cables and struts are geometrically equivalent, respectively. The end of each strut is connected to four cables. The cables together with struts constitute an icosahedron, which has eight closed equilateral triangles and 12 open isosceles triangles on the surface (Figure S2 and Table S1, Supporting Information). The eight closed triangles can be further classified into four clockwise triangles and four anticlockwise triangles depending on the twisting direction of the three connected struts. Each cable is shared by one closed triangle and one open triangle. Based on the geometrical analysis shown in the Supporting Information, the ratio between the length of the cable l_{cable} and the length of the strut l_{strut} of the tensegrity structure reaches a minimum value of 0.61,

Dr. Z. Wang, Prof. K. Li, Q. He, Prof. S. Cai
Department of Mechanical and Aerospace Engineering
University of California, San Diego
La Jolla, CA 92093, USA
E-mail: shqcai@ucsd.edu

Prof. K. Li
Department of Civil Engineering
Anhui Jianzhu University
Hefei, Anhui 230601, China

Prof. S. Cai
Materials Science and Engineering Program
University of California, San Diego
La Jolla, CA 92093, USA

 The ORCID identification number(s) for the author(s) of this article can be found under <https://doi.org/10.1002/adma.201806849>.

DOI: 10.1002/adma.201806849

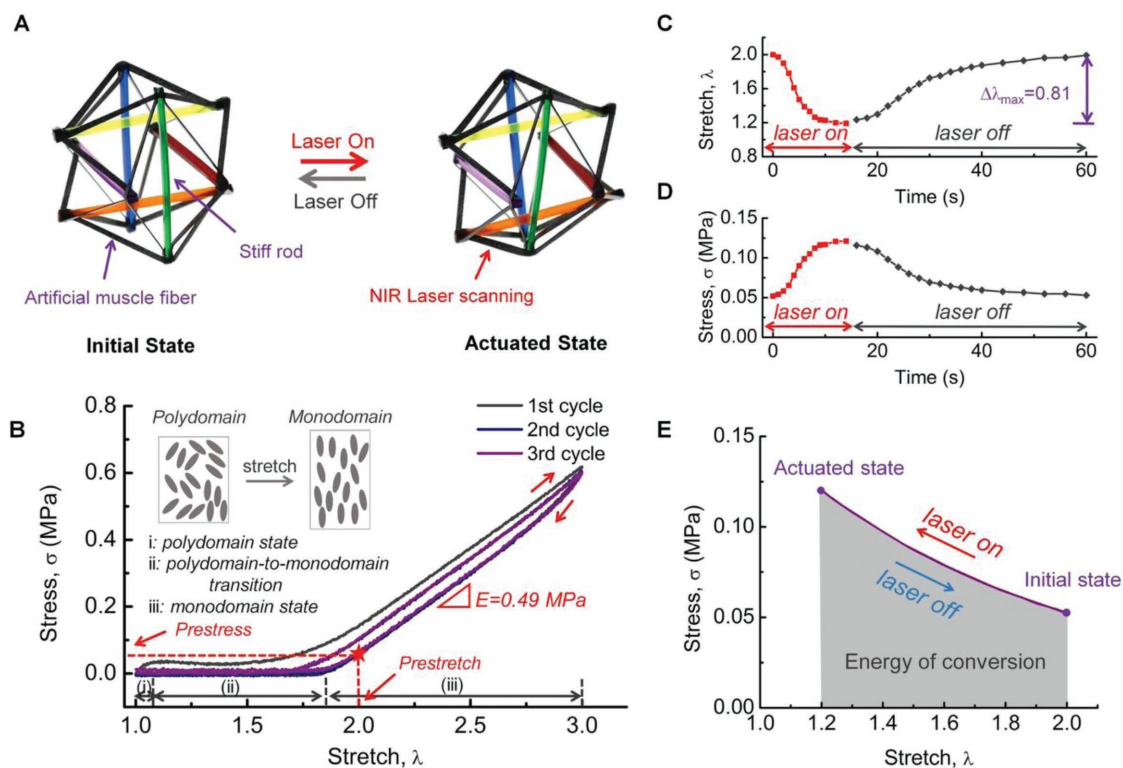


Figure 1. Light-induced deformation of a tensegrity robot. A) The configurations of the tensegrity robot before and after the light-induced contraction of one artificial muscle fiber. The length of the strut in tensegrity robot is 6 cm. B) The loading–unloading stress versus stretch diagram of an LCE–CNT composite fiber. The star-shaped point indicates the initial prestressed state of the fiber in the robot. C) The time-dependent stretch of the actuated artificial muscle fiber in the tensegrity robot upon NIR laser scanning. The maximum stretch change can be as large as 0.81 (i.e., 41% of contraction of the initial length). D) The time-dependent stress in the actuated cable in the tensegrity robot upon NIR laser scanning. E) The stress and stretch in the actuated cable during the laser irradiation and after the laser is off.

if all the cables are in prestressed state. The tensegrity robot is entirely made up of polymers with large free space, which makes it ultralight compared with conventional robots. The effective mass density of the tensegrity robot can be estimated as $\bar{\rho} \sim \rho l w t / l^3 = \rho w t / l^2$, where l is the length, w is the width, t is the thickness, and ρ is the density, of the cable or the strut. The above scaling shows that the average mass density can be much smaller than the density of its constituent material $\bar{\rho} \ll \rho$, for $w, t \ll l$. For the tensegrity robot constructed in the current work, the effective mass density is around 50 kg m^{-3} , which is only 5% of the density of water, and much lighter than previously reported robots, attributing to the large free space in the structure.

The deformability of the tensegrity robot is mainly determined by the mechanical properties of the stretchable tensional cables. Figure 1B shows the loading–unloading stress versus stretch diagram of an LCE–CNT composite fiber. Mesogens in the as-prepared LCE–CNT composite fibers are in polydomain nematic state. When the fiber is stretched, the mesogens rotate gradually to align in the stretching direction. Such stretch-induced rotation and alignment result in a stress plateau as shown in Figure 1B, which is often called semisoft elasticity.^[22] The transition from polydomain state to a well-aligned monodomain state completes when the applied stretch reaches 1.8, beyond which, the stress increases significantly with the stretch. As shown in Figure 1B, when a greatly stretched

LCE–CNT composite fiber is fully unloaded, large plastic strain is remained, which enables a free-standing fiber to stay in monodomain state. During the fabrication of the tensegrity robot, large stretch (typically around 2.5) is first applied onto the LCE–CNT fibers, which are then partially unloaded after the construction of the tensegrity robot. Detailed discussion of the fabrication process and the geometry of the tensegrity robot is given in the Supporting Information. The initial state of the LCE–CNT composite fiber in the tensegrity robot is marked by a star-shaped dot in Figure 1B with an initial prestretch around 2, unless specifically stated otherwise. The tensile prestress in the fiber is important for preserving the shape of the tensegrity robot with carrying large load (Figure S3, Supporting Information).

Because the LCE–CNT composite fibers in the tensegrity robot are initially in monodomain states induced by prestress, they can contract significantly through nematic-to-isotropic phase transition of mesogens when the temperature is raised above a critical value.^[23–26] The actuating stress of an LCE–CNT composite fiber with a fixed strain can reach 0.24 MPa under NIR laser irradiation for 3 s (Figure S1C, Supporting Information), which is large enough to induce large deformation of the tensegrity robot. In the experiment, we hang the tensegrity robot in air and use an NIR laser to scan along one of the LCE–CNT composite fibers remotely and measure its time-dependent contraction. With the laser irradiation, the

embedded CNTs in the fiber can absorb light, convert it to heat, and induce the contraction of the fiber as shown in Figure 1A. The change of the stretch of the actuated fiber with the increase of laser irradiating time is shown in Figure 1C. Within 14 s, the fiber contracts from the initial prestretch of 2 to the stretch of 1.19; the fiber recovers to its initial length within 30 s after the laser is turned off. Such large and reversible light-driven deformation is one of the unique advantages of LCE, as a recently emerging artificial muscle material.^[20,21] The contracting and recovery speeds are comparable to previously reported LCE-based soft robots.^[27,28] During the contraction of the actuated fiber, all the other passive LCE–CNT composite fibers are stretched, and the tensegrity structure deforms. Based on the stress versus stretch diagram of a passive LCE–CNT composite fiber as shown in Figure 1B, we can calculate the corresponding actuating stress generated by the actuated fiber during the laser irradiation as plotted in Figure 1D. The detailed calculations can be found in the Supporting Information. With neglecting all the damping effects of the passive parts of the tensegrity structure such as viscoelasticity of the cables, we can obtain an overlapped curve of stress and stretch of the actuated LCE–CNT fiber for both of the duration with laser irradiation and after the laser is off (Figure 1E). In reality, a hysteretic loop should be more accurate to describe the actuating stress and actuating stretch of the cable under laser irradiation and after the laser is off. Based on Figure 1E, under the light irradiation, the LCE–CNT fiber absorbs light and conduct mechanical work to the rest part of the tensegrity robot. The energy of conversion realized by the actuated cable can reach 66 kJ m^{-3} , which is comparable to that of mammalian skeletal muscle.^[29]

We next explore light-powered multidirectional rolling of the tensegrity robot through the actuation of one LCE–CNT composite fiber. The robot can stand stably on the ground with one of its 20 triangles as its base of support. When one cable of the tensegrity structure contracts, the line of gravity of the robot may move outside its base of support and the structure rolls. Our theoretical analysis (Figure S4, Supporting Information) shows that a minimal contraction is needed for a specific cable to drive robot to roll: if the base of support is a closed triangle, we need to generate the contraction in the cable that is one edge of the base triangle at least by 35.9% of its initial length to trigger the rolling (Figure S5A and Table S2, Supporting Information); if the base of support is an open triangle, we need to generate the contraction in the cable which is one edge of the neighboring open triangle at least by 28% of its initial length to trigger the rolling (Figure S5B and Table S3, Supporting Information). We next use an NIR laser to scan along the corresponding cable by following the theoretical analysis above. The contraction of the actuated cable in the tensegrity robot is recorded upon different laser scanning time as shown in Figure 2A,B. Subject to NIR laser scanning, the actuated cable contracts and the tensegrity robot deforms and finally rolls. The measured critical stretch of the actuated cable for triggering the rolling is 1.28 (i.e., 36% contraction of its initial length) for a closed triangle base and 1.34 (i.e., 33% contraction of its initial length) for an open triangle base. The measured contractions are both slightly larger than the theoretical predictions. We can further calculate the stress in the actuated cable and the energy of conversion through the method described previously. During

one rolling step, the energy of conversion is 56 kJ m^{-3} for a closed triangle base and 40 kJ m^{-3} for an open triangle base (Figure S6, Supporting Information).

It is known that structural compliance of a tensegrity structure highly depends on the magnitude of the prestress in the tensional cables.^[13] Therefore, we can also tailor the compliance of the tensegrity robot by changing the prestress in the artificial muscle fibers, which can be useful in practical applications. We next study how the prestress affects the rolling performance of the tensegrity robot. We built several tensegrity robots with different initial prestress. Figure S7 in the Supporting Information shows the comparison between theoretical predictions and experimental measurements of the critical contractions for triggering the rolling of the robot with different initial prestress. We find that the critical contraction of the actuated cable increases slightly (i.e., the critical stretch decreases) with the increase of prestress. When the prestress in the cable is beyond 2.3, the cable breaks before driving the robot to roll.

We next use a digital camera and IR thermal imaging camera to capture the light-powered rolling process of the tensegrity robot (Figures S8 and S9, Supporting Information). With the cable being actuated, the robot with open triangle base rolls to a state with the neighboring closed triangle as its base; if the base of the robot is a closed triangle, it undertakes two-step continuous rolling to the state with another closed triangle as its base, with a short stopover in an intermediate state with an open triangle base. The theoretical analysis shows that the two-step continuous rolling results from the large rolling inertia of the tensegrity robot (Figure S10, Supporting Information). We have verified the light-powered rolling rules in the tensegrity robot for each one of the 20 triangles as its base of support (Figures S11–S13, Supporting Information). Because of the rolling rules described above, the initial base of the tensegrity robot only affects its first-step rolling. The subsequent rolling of the robot can be always depicted by the transition of one closed triangle to another as shown in Figure 2C.

Most previously developed active material-based robots can only move along one or two predetermined paths, and their initial configurations are very important for its locomoting capability. Thanks to the 3D distributions of multiple artificial muscle fibers, the tensegrity robot built in the current work can roll to multiple directions and along numerous paths, regardless of its initial configuration. This is essential for enhancing the moving capability of a robot in complex environments where randomly distributed obstacles or traps may exist. Based on the correspondence between the actuating cable and rolling direction of the robot as shown in Figure 2D, we can precisely drive the robot to move along many different paths. If the position of the robot is marked by the center of its base triangle, the possible locomoting paths of it form a hexagonal pattern as shown in Figure 2E. The tensegrity robot can reach any one of the crossing points of the hexagonal pattern through multiple steps of one-cable actuation. Here, we demonstrate two controlled rolling paths of the robot powered by light: zigzag path AA' and a turn-around path BB' with a turning radius of 3.98 cm (or 0.66 body length) in Figure 2F,G and Movies S1 and S2 in the Supporting Information. We marked the center of the base triangle of the robot by a purple point to show its position after laser scanning of each time. We can

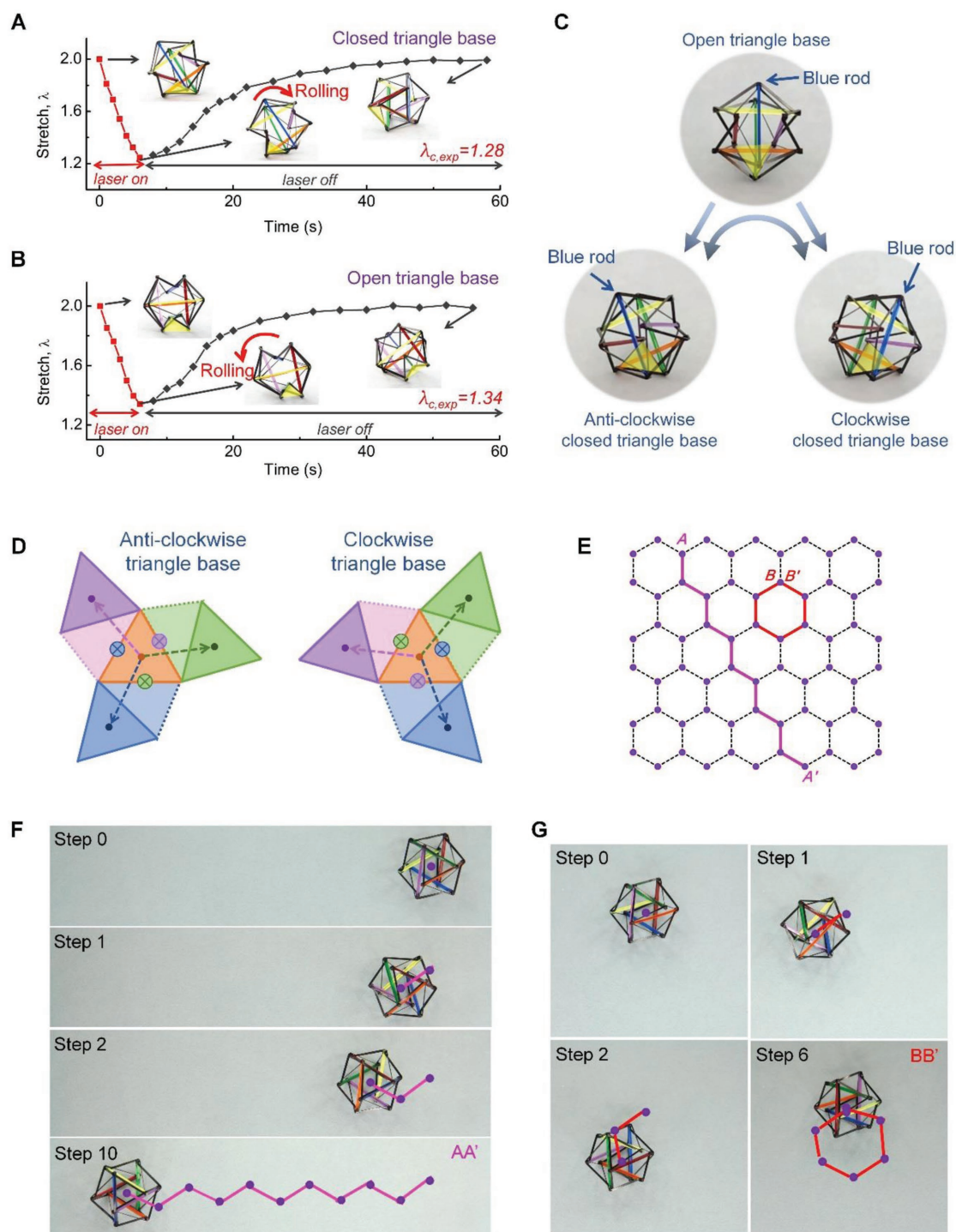


Figure 2. Light-induced controllable multidirectional rolling of the tensegrity robot. The time-dependent stretch of the actuated cable upon NIR laser scanning in the tensegrity robot with a closed triangle base A) and open triangle base B), respectively. The initial base of support of the robot is marked by light yellow. C) With light-induced actuation, base of support of the robot transits between an open triangle and a (anticlockwise or clockwise) closed triangle. With single-cable actuation, the tensegrity robot with an open triangle as its base of support can roll to the state with either a clockwise or anticlockwise closed triangle as its base, while the robot with a (clockwise or anticlockwise) closed triangle as the base of support undertakes two-step continuous rolling to another state with a (anticlockwise or clockwise) closed triangle as its base of support, with an open triangle base as an intermediate state. The position of blue rod in each state is marked with an arrow. D) The control of the multidirectional rolling of the robot through single-cable actuation. The middle orange triangle is the initial base of support of the robot. When a cable marked by a colored cross is actuated, the robot rolls two steps to the state with a solid triangle of the same color as its base. E) We use the center of the base of the support of robot to present its position. With single-cable actuation, all the possible positions of the robot form a hexagonal pattern. F) The demonstration of the zigzag rolling path of the robot powered by light. G) The demonstration of a turn-around rolling path of the robot powered by light. The length of the strut in the tensegrity robot is 6 cm.

also drive the robot to move in a maze at a speed of $1.15 \text{ body length min}^{-1}$ (6.87 cm min^{-1}) as shown in Movie S3 in the Supporting Information.

A tensegrity structure has also been known for its excellent deployability, resilience, impact-mitigation capability, and large empty space inside. Those features fit extremely well to the applications of robotics. As shown in Figure S14 and Movie S4 in the Supporting Information, the tensegrity robot built in the current work can be tightly packed under compression and completely recover to its initial state after the compression is removed, which is highly desired for the applications in space engineering. To accomplish real tasks, additional functional devices usually need to be loaded onto the locomoting robot. Compared to conventional hard robots, the load-carrying ability of soft-bodied robots are often too low. In the ultralight hybrid

tensegrity robot, we load additional weight of 7.5 times of the weight of the robot as shown in Figure 3A. The light-powered locomotion of the tensegrity robot with the additional load is almost unaffected (Movie S5, Supporting Information). The large free space and high loading capacity make tensegrity robots a perfect platform for accommodating large and heavy cargos. In Figure 3B, we plot the load-carrying ability of the hybrid tensegrity robot together with many previously developed soft and hard robots.^[10,30–40] As we can see from Figure 3B, although the tensegrity robot constructed in the current work is highly deformable, its load capacity is much higher than many other soft-bodied robots and also hard robots of similar weight. In addition to carrying the load, we show that the high resilience of the tensegrity robot can also be harnessed to protect a fragile cargo against impact. As shown in Figure 3C and Figure S15

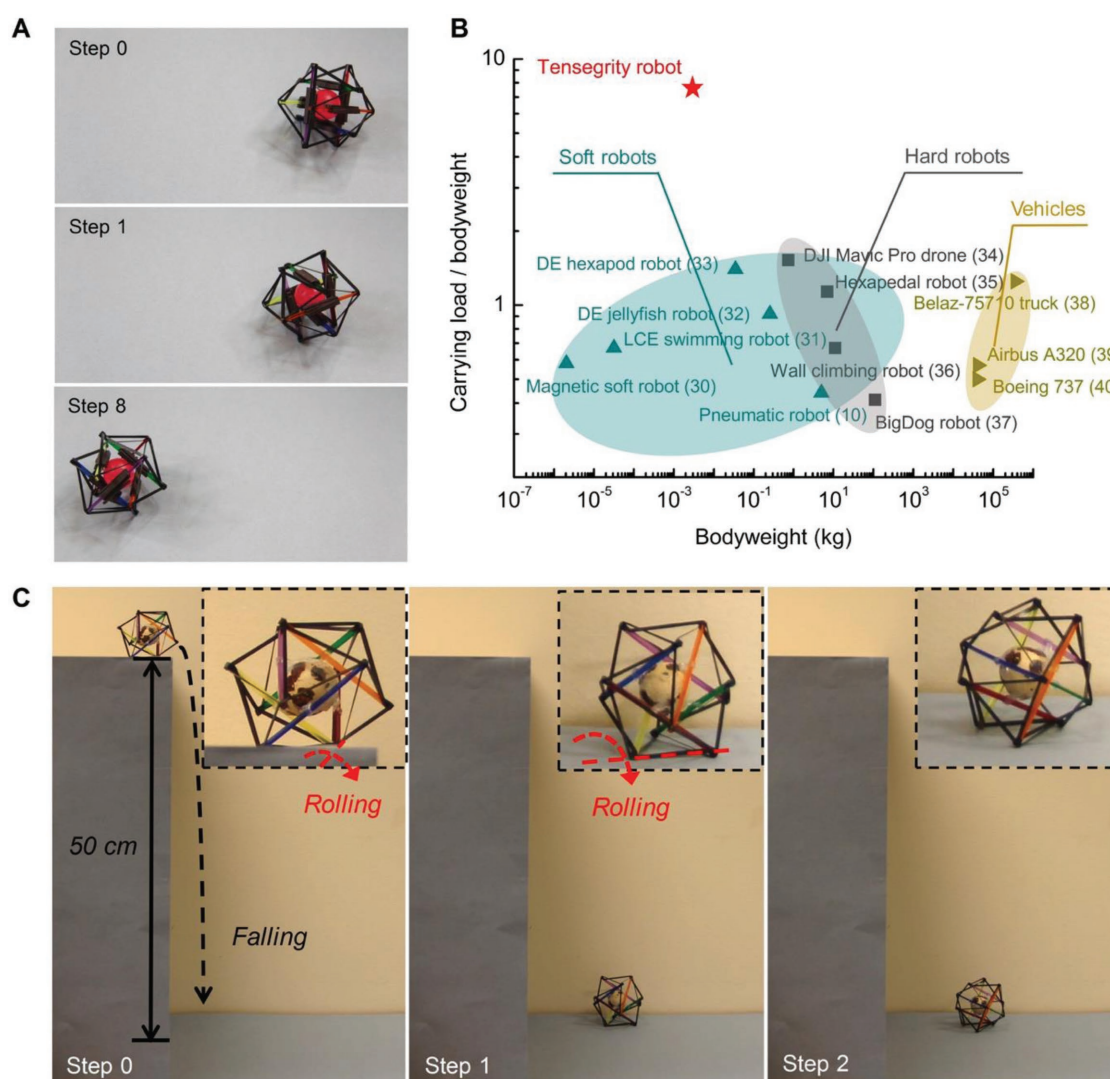


Figure 3. Rolling of the tensegrity robot with carrying a cargo. A) Light-induced rolling of the tensegrity robot carrying a cargo, which is 7.5 times heavier than the weight of the robot. The length of the strut in the tensegrity robot is 6 cm. B) Specific load capacity versus bodyweight of several previously developed robots. DE and LCE in the plot represent dielectric elastomer and LCE, respectively. C) The tensegrity robot can also protect a fragile cargo (represented by a raw quail egg) after falling down. Inset: the magnified photos of the tensegrity robot. The tensegrity robot carries a fragile raw quail egg and is placed on an edge of a table of half meter height. It rolls under light actuation and falls from the desk. The egg is protected by the tensegrity robot from damage and the robot keeps the rolling capability after falling. The length of the strut in the tensegrity robot is 7.2 cm.

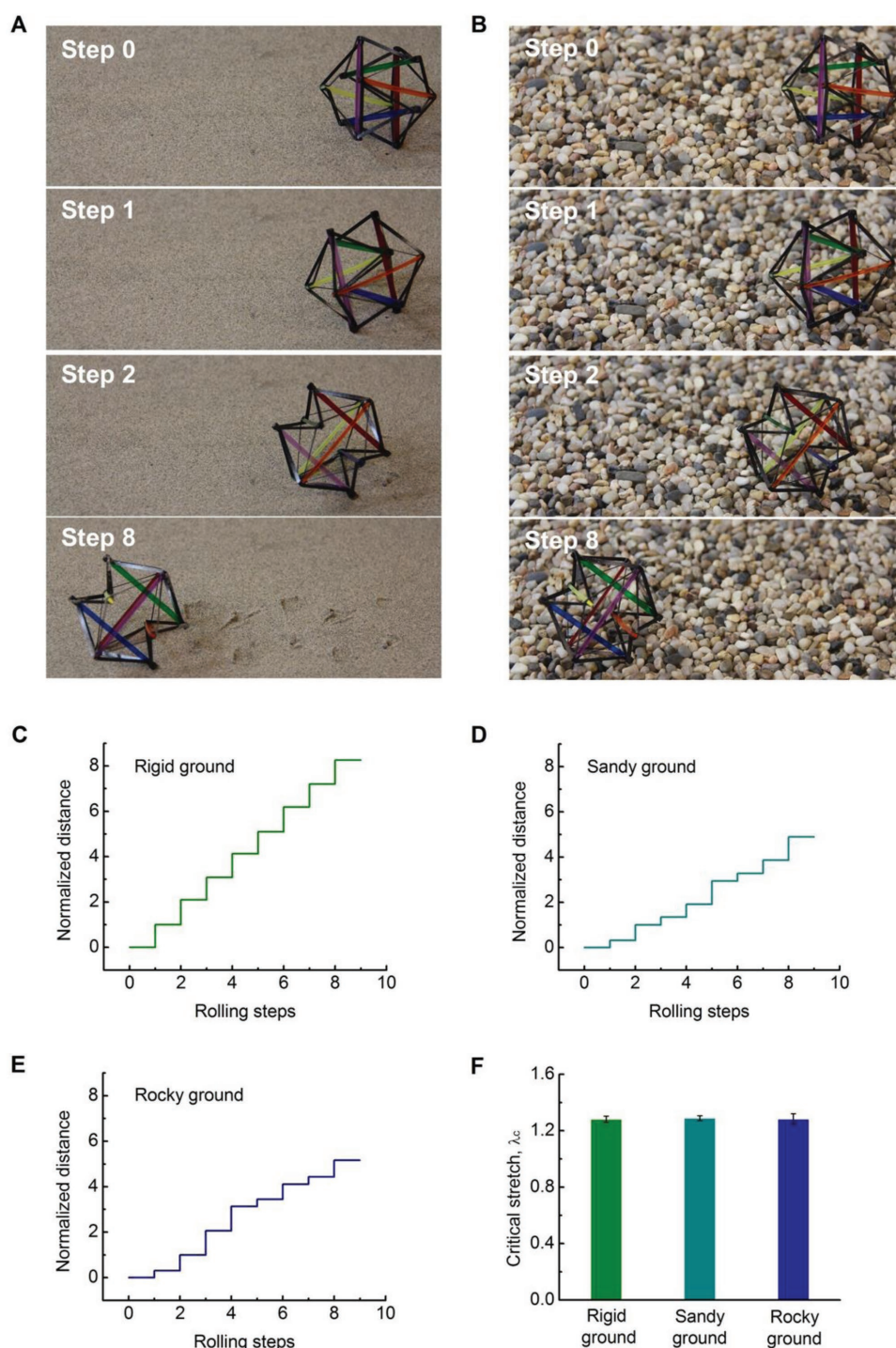


Figure 4. Light-induced rolling of the tensegrity robot on various terrains. A) Light-induced rolling of the robot on a sandy surface. B) Light-induced rolling of the robot on a rocky surface. C–E) The normalized rolling distance versus rolling steps on rigid flat ground, sandy ground, and rocky ground, respectively. The rolling distance is defined as the accumulation of the projection length of each step along the moving direction of zigzag path AA' normalized by the projection length of two-step continuous rolling. On sandy and rocky ground, the robot may take one-step rolling to a state with open triangle base occasionally. F) The measured critical stretch of the actuated cable for driving the robot to roll on various grounds. The length of the strut in the tensegrity robot A,B) is 6 cm.

in the Supporting Information, a raw quail egg carried by the tensegrity robot remains intact after falling down from a table of half-meter height. The performance of the light-powered rolling of the tensegrity robot is also unaffected due to the drop.

Finally, we demonstrate that the tensegrity robot can roll on multiterrains. It has been well known that it is challenging for a robot to move on many natural substrates which can flow when its yield stress is exceeded, like sand, gravel, soil, mud,

snow, grass, and leaf litter. Light weight is crucial for a robot to move on those easily deformable surfaces. For instance, a zebra-tailed lizard can run easily on the sands by only penetrating a small portion of its limbs into deformable substrates because of its light weight.^[41,42] In the experiment, we place the tensegrity robot on the surfaces of both beach sands (with a porosity of 51%) and gravels. As shown in **Figure 4A,B**, we can still easily drive the rolling of tensegrity robot on both substrates (Movies S6 and S7, Supporting Information). Compared with stiff and solid ground, the robot may undertake one-step rolling to a state with an open triangle as its base of support on the sands and gravels, because of the irregularity of the surfaces (**Figure 4C–E**). The rolling distance per step of the robot on these irregular surfaces can be smaller than that on the flat rigid ground. However, the critical actuating contractions of the active cable to enable the rolling of the robot on different substrates are almost the same, as shown in **Figure 4F**, implying that there are no intrinsic difficulties for us to use light to drive the tensegrity robot to move on solid, sandy or gravel ground.

In summary, inspired by the musculoskeletal system of animals, we combine soft and stretchable artificial muscle fibers with stiff plastic rods to construct an untethered tensegrity robot. The hybrid robot is highly scalable and can be entirely powered by light to move on various terrains along many different paths with carrying heavy cargos. Additionally, the robot is highly deployable and able to protect fragile cargos against impact. It is reasonable to expect that certain performance of the tensegrity robot such as moving speed can be further improved by optimizing the structural design and material selection. Furthermore, although in this article, only light-powered locomotion of a tensegrity robot has been demonstrated, we believe LCE-based tensegrity robots with many other functionalities such as light-powered gripping and manipulation can be designed and fabricated, possibly with the inspirations from certain biological structures.

Supporting Information

Supporting Information is available from the Wiley Online Library or from the author.

Acknowledgements

Z.W. and K.L. contributed equally to this work. The authors acknowledge support from the National Science Foundation through Grant No. CMMI-1554212 and ONR through Grant No. N00014-17-1-2062. K.L. acknowledges the support from National Natural Science Foundation of China (Grant No. 11402001). The authors thank Qingyang Wang for help on thermal measurement and acquiring IR images.

Conflict of Interest

The authors declare no conflict of interest.

Keywords

liquid crystal elastomers, robots, tensegrity

Received: October 22, 2018

Revised: December 1, 2018

Published online: December 21, 2018

- [1] G. M. Whitesides, *Angew. Chem., Int. Ed.* **2018**, *57*, 4258.
- [2] F. Ilievski, A. D. Mazzeo, R. F. Shepherd, X. Chen, G. M. Whitesides, *Angew. Chem.* **2011**, *123*, 1930.
- [3] R. F. Shepherd, F. Ilievski, W. Choi, S. A. Morin, A. A. Stokes, A. D. Mazzeo, X. Chen, M. Wang, G. M. Whitesides, *Proc. Natl. Acad. Sci. U S A* **2011**, *108*, 20400.
- [4] D. Rus, M. T. Tolley, *Nature* **2015**, *521*, 467.
- [5] Y. L. Park, B. Chen, N. O. Pérez-Arancibia, D. Young, L. Stirling, R. J. Wood, E. C. Goldfield, R. Nagpal, *Bioinspiration Biomimetics* **2014**, *9*, 016007.
- [6] M. Wehner, R. L. Truby, D. J. Fitzgerald, B. Mosadegh, G. M. Whitesides, J. A. Lewis, R. J. Wood, *Nature* **2016**, *536*, 451.
- [7] L. Yu, H. Yu, *ACS Appl. Mater. Interfaces* **2015**, *7*, 3834.
- [8] J. Hu, X. Li, Y. Ni, S. Ma, H. Yu, *J. Mater. Chem. C* **2018**, *6*, 10815.
- [9] A. A. Stokes, R. F. Shepherd, S. A. Morin, F. Ilievski, G. M. Whitesides, *Soft Rob.* **2014**, *1*, 70.
- [10] M. T. Tolley, R. F. Shepherd, B. Mosadegh, K. C. Galloway, M. Wehner, M. Karpelson, R. J. Wood, G. M. Whitesides, *Soft Rob.* **2014**, *1*, 213.
- [11] A. J. Ijspeert, *Science* **2014**, *346*, 196.
- [12] S. Oka, T. Tomita, K. Miyamoto, *PLoS One* **2016**, *11*, e0166108.
- [13] R. E. Skelton, R. Adhikari, J.-P. Pinaud, W. Chan, J. W. Helton, *Proc. of the 40th IEEE Conf. on Decision and Control, IEEE Decis. Contr. P.* **2001**, *5*, 4254.
- [14] K. Kim, A. K. Agogino, D. Moon, L. Taneja, A. Toghyhan, B. Dehghani, V. SunSpiral, A. M. Agogino, *IEEE Int. Conf. Rob. Biomimetics* **2014**, *p. 7*.
- [15] A. P. Sabelhaus, J. Bruce, K. Caluwaerts, P. Manovi, R. F. Firoozi, S. Dobi, A. M. Agogino, V. SunSpiral, *IEEE Int. Conf. Rob. Autom. (ICRA)* **2015**, 2867.
- [16] L.-H. Chen, K. Kim, E. Tang, K. Li, R. House, E. L. Zhu, K. Fountain, A. M. Agogino, A. Agogino, V. SunSpiral, *J. Mechan. Rob.* **2017**, *9*, 025001.
- [17] Y. Koizumi, M. Shibata, S. Hirai, *IEEE Int. Conf. Rob. Autom. (ICRA)* **2012**, *p. 1988*.
- [18] S. Hirai, Y. Koizumi, M. Shibata, M. Wang, L. Bin, *IEEE/ASME Int. Conf. Adv. Intell. Mechatronics (AIM)* **2013**, *p. 19*.
- [19] M. Shibata, F. Saijyo, S. Hirai, *IEEE Int. Conf. Rob. Autom. (ICRA)* **2009**, *p. 4375*.
- [20] C. Ohm, M. Brehmer, R. Zentel, *Adv. Mater.* **2010**, *22*, 3366.
- [21] T. J. White, D. J. Broer, *Nat. Mater.* **2015**, *14*, 1087.
- [22] T. H. Ware, J. S. Biggins, A. F. Shick, M. Warner, T. J. White, *Nat. Commun.* **2016**, *7*, 10781.
- [23] H. Tian, Z. Wang, Y. Chen, J. Shao, T. Gao, S. Cai, *ACS Appl. Mater. Interfaces* **2018**, *10*, 8307.
- [24] D. L. Thomsen, P. Keller, J. Naciri, R. Pink, H. Jeon, D. Shenoy, B. R. Ratna, *Macromolecules* **2001**, *34*, 5868.
- [25] Z. Pei, Y. Yang, Q. Chen, E. M. Terentjev, Y. Wei, Y. Ji, *Nat. Mater.* **2014**, *13*, 36.
- [26] Q. He, Z. Wang, Z. Song, S. Cai, *Adv. Mater. Technol.* **2018**, *3*, 1800244.
- [27] M. Rogóż, H. Zeng, C. Xuan, D. S. Wiersma, P. Wasylczyk, *Adv. Opt. Mater.* **2016**, *4*, 1689.
- [28] C. Wang, K. Sim, J. Chen, H. Kim, Z. Rao, Y. Li, W. Chen, J. Song, R. Verduzco, C. Yu, *Adv. Mater.* **2018**, *30*, 1706695.
- [29] S. M. Mirvakili, I. W. Hunter, *Adv. Mater.* **2018**, *30*, 1704407.
- [30] W. Hu, G. Z. Lum, M. Mastrangeli, M. Sitti, *Nature* **2018**, *554*, 81.
- [31] C. Huang, J. Lv, X. Tian, Y. Wang, Y. Yu, J. Liu, *Sci. Rep.* **2015**, *5*, 17414.
- [32] H. Godaba, J. Li, Y. Wang, J. Zhu, *IEEE Rob. Autom. Lett.* **2016**, *1*, 624.
- [33] C. T. Nguyen, H. Phung, T. D. Nguyen, H. Jung, H. R. Choi, *Sens. Actuators, A* **2017**, *267*, 505.

- [34] Mavic Pro core specs, <https://www.dji.com/mavic/info> (accessed: December 2018).
- [35] U. Saranli, M. Buehler, D. E. Koditschek, *Int. J. Robotics Research* **2001**, 20, 616.
- [36] J. Xiao, B. Li, K. Ushiroda, Q. Song, *IEEE Int. Conf. Rob. Biomimetics* **2015**, p. 2072.
- [37] <https://www.bostondynamics.com/bigdog> (accessed: December 2018).
- [38] <http://www.belaz.by/en/catalog/products/dumptrucks/7571/75710/> (accessed: December 2018).
- [39] https://www.airbus.com/content/dam/corporate-topics/publications/backgrounders/techdata/aircraft_characteristics/Airbus-Commercial-Aircraft-AC-A320-Feb18.pdf (accessed: August 2018).
- [40] https://www.boeing.com/resources/boeingdotcom/company/about_bca/startup/pdf/historical/737-classic-passenger.pdf (accessed: December 2018).
- [41] C. Li, S. T. Hsieh, D. I. Goldman, *J. Exp. Biol.* **2012**, 215, 3293.
- [42] T. Zhang, F. Qian, C. Li, P. Masarati, A. M. Hoover, P. Birkmeyer, A. Pullin, R. S. Fearing, D. I. Goldman, *Int. J. Rob. Res.* **2013**, 32, 859.